Deficient $Bi_{24}O_{31}Br_{10}$ as a highly efficient photocatalyst for selective oxidation of benzyl alcohol into benzaldehyde under blue LED irradiation

Xin Xiao*, Chunxia Zheng, Mingli Lu, Ling Zhang, Fei Liu, Xiaoxi Zuo, Junmin Nan*

School of Chemistry and Environment, South China Normal University, Guangzhou 510006, PR China

ARTICLE INFO

ABSTRACT

The selective oxidation of benzyl alcohol (BA) into benzaldehyde (BAD) is an attractive model reaction for organic synthesis. Using a microwave-calcination route, a novel flower-like $Bi_{24}O_{31}Br_{10}$ with surface oxygen vacancies and bromine vacancies was successfully synthesized. In the construction of $Bi_{24}O_{31}Br_{10}$, glucose acts as a complexing, reducing, and structure-directing agent. The as-synthesized $Bi_{24}O_{31}Br_{10}$ exhibits excellent activity for the photocatalytic aerobic oxidation of BA into BAD, with > 99% conversion and > 99% selectivity under blue LED irradiation at ambient conditions, which is 3.3-, 4.7-, and 27.8-fold higher than that of TiO_2, $Bi_4O_5Br_2$, and $Bi_{12}O_{17}Cl_2$, respectively. The high selectivity is due to the suitable energy band of the as-synthesized $Bi_{24}O_{31}Br_{10}$ (E_g = 2.51 eV, valence band potential = +2.38 V), while the high conversion rate is largely due to the efficient separation of photogenerated carriers, surface defects, positively charge surface, and 3D micro/nano-architecture. The primary active species, including h^+, e^-, $\cdot O_2^-$, and $\cdot OH$, are all involved in the photoreaction. On the basis of experimental results and quantum-chemistry calculations, a direct hole oxidative mechanism with two-step dehydrogenation pathway was suggested. In addition, the as-synthesized $Bi_{24}O_{31}Br_{10}$ catalyst remains stable during the photocatalytic process, indicating its potential for practical applications.

1. Introduction

Since Fujishima and Honda first discovered photocatalytic water splitting on a TiO_2 electrode in 1972 [1], semiconductor photocatalysis has received tremendous attention and is considered one of the most promising strategies for solar energy harvesting [2], environmental remediation [3], and clean fuel production [4,5]. Recently, investigators have focused on photocatalytic selective synthesis because it is recognized as an alternative, green, and sustainable pathway for the fabrication of valuable compounds under mild conditions [6]. However, since the reactions between photogenerated species and organics are generally complex and nonselective, resulting in the formation of multiple products or degradation, the success stories of selective photocatalytic conversions are still limited [7].

As an important industrial chemical, benzaldehyde (BAD) is used extensively as a raw material and intermediate in the synthesis of a range of pharmaceuticals, perfumes, dyestuffs, and other fine chemicals [8]. Traditional industrial procedures for the synthesis of BAD through the oxidation of toluene or the hydrolysis of benzyl chloride not only utilize hazardous or corrosive reagents, such as chromates, permanganates, hypochlorite, and Br_2, they also release considerable quantities of toxic by-products after production [9]. Therefore, a green,

environmentally friendly route for the synthesis of BAD is urgently needed. Recently, the photocatalytic selective oxidation of benzyl alcohol (BA) into BAD has attracted wide attention because it appears to meet the above requirements and may improve the understanding of the basic reaction mechanism for organic transformations [10].

Till now, photocatalytic partial oxidation of BA to BAD has been successively developed over photocatalysts such as TiO_2 [11], g-C_3N_4 [12], WO_3 [8], CdS [13], MoS_2 [14], Bi_2WO_6 [15], and Bi_2MoO_6 [16], under UV or visible light irradiation. Unfortunately, the photocatalytic aerobic oxidation of BA in these processes is still suffers from low efficiency or poor selectivity. To overcome these drawbacks, novel photocatalysts should be further developed, and some important aspects should be considered. First, since the photogenerated hole (h^+) is the only selective oxidative species in photocatalytic processes, photocatalysts should have suitable valence band (VB) potentials with sufficient oxidizing power for the oxidation of BA into BAD. However, they should also prevent over-oxidation of BAD or the direct formation of hydroxyl radicals ($\cdot OH$, highly active, high oxidation capacity, and nonselective oxidative species) [17] to realize a high selectivity. In addition, to achieve a high efficiency and conversion ratios, photocatalysts should fully utilize visible light (which accounts for more than half of the solar spectrum), effectively generate and utilize

---

photogenerated carriers, and strongly interact with reactants (BA and O_2; by adsorption, electrostatic effect, or bonding), while weakly interacting with the reaction products (BAD and H_2O).

As typical V-VI-VII ternary semiconductors, bismuth oxyhalides (BiOX, X = Cl, Br, and I) have revealed outstanding photocatalytic performances for the degradation of various environmental contaminants, owing to their unique crystal structures, energy band structures, and excellent stability. More importantly, oxygen-rich BiOX and BiOX solid solutions with desired VB potentials can be obtained by tuning the Bi:O:X ratios and type of X [18], and these photocatalysts cannot readily produce ·OH under visible light due to the relatively low redox potential of Bi^{5+}/Bi^{3+}. Thus, they may be promising candidates for photocatalytic selective oxidation. In 2013, Zhang's group first described the photocatalytic oxidation of BA into BAD on $Bi_{12}O_{17}Cl_2$ nanobelts under visible light irradiation, and a > 99% selectivity with > 44% conversion rate were attained [19]. Afterward, Ding et al. reported BiOCl hexagonal prisms as a photocatalyst for partial oxidation of BA under both UV and visible light [20]. Then, a > 99% selectivity and > 40% conversion over $Bi_{24}O_{31}Cl_{10}/BiOCl$ heterojunctions were demonstrated by Liu et al. [21]. In a previous study, our group reported a remarkable performance (> 99% selectivity and > 99% conversion) for the photocatalytic oxidation of BA into BAD on $Bi_4O_5Br_2$ under irradiation with blue light emitting diodes (LED, an energy-efficient artificial light source) [22]. Very recently, the photocatalytic conversion of BA into BAD was investigated over the Au/BiOCl with oxygen vacancies under visible light, a > 99% selectivity and 75.6% conversion were demonstrated [17]. Also, Fe(III)-modified BiOBr showed satisfactory photocatalytic activity for BA oxidation in the presence of H_2O_2 and UV-light illumination [23].

Here, a 3D flower-like $Bi_{24}O_{31}Br_{10}$ was successfully synthesized through a microwave-calcination route. The as-prepared $Bi_{24}O_{31}Br_{10}$ has both oxygen vacancies (OV) and bromine vacancies (BrV) and revealed an excellent photocatalytic performance for the selective conversion of BA into BAD under blue LED light irradiation at ambient conditions with a > 99% selectivity and > 99% conversion in a short reaction time (2.5 h). The formation mechanism of the as-synthesized deficient $Bi_{24}O_{31}Br_{10}$ and the photocatalytic mechanism of the partial oxidation of BA were analyzed and discussed according to the experimental results and quantum chemical calculations.

2. Experimental

2.1. Materials and methods

Bismuth nitrate pentahydrate ($Bi(NO_3)_3 \cdot 5H_2O$), potassium bromide (KBr), and glucose monohydrate ($C_6H_{12}O_6 \cdot H_2O$) were obtained from the Tianjin Kermel Chemical Reagent Co. Ltd. Ethylene glycol (EG) was purchased from China Sun Specialty Products Co. Ltd. Benzyl alcohol (BA) and benzaldehyde (BAD) were purchased from the Beijing Chemical Reagent Co., Ltd. Acetonitrile was bought from J&K Chemical, Ltd. All chemicals were of analytical grade and used without further purification.

In a typical synthesis, a precursor was firstly prepared by a simple microwave route. Initially, 6 mmol of $C_6H_{12}O_6 \cdot H_2O$ was completely dissolved in 50 mL EG. Then, 1.0 mmol of $Bi(NO_3)_3 \cdot 5H_2O$ and 0.5 mmol of KBr were successively added to the above solution. After continuous magnetic stirring for another 12 h at room temperature, the clear solution was transferred into a 150 mL flat-bottom flask and heated for 4 min at 400 W power in a microwave chemical reactor (MCR-3, Beijing Rui Chengwei Industry Equipment Co., Ltd., China) under atmospheric pressure. When the system is cooling down to room temperature, the tawny products were collected by centrifugation, washed several times with deionized water and absolute ethanol, and then dried at 60 °C in an oven. Lastly, the $Bi_{24}O_{31}Br_{10}$ products were obtained by calcining the precursor in a furnace at 450 °C for 3 h under air atmosphere.

For comparison, six $Bi_{24}O_{31}Br_{10}$ samples were synthesized

individually by reported methods in the literature [24–29] (labeled S2 to S7 in sequence); a $Bi_{12}O_{17}Cl_2$ sample was prepared using the technique developed by Zhang's group [19]; a $Bi_4O_4Br_2$ sample was synthesized according to the method reported in our previous work [22]; and nano-TiO_2 was purchased from the Aladdin Reagent Co. Ltd., Shanghai, China.

2.2. Evaluation of photocatalytic activities

The photocatalytic oxidation of BA over the synthesized samples was performed in a homemade LED photoreactor (Scheme S1, Supporting information) at atmospheric pressure and room temperature without extra air/oxygen purging. A 100 mL quartz beaker was used as the reaction vessel, and blue LED lamps (0.5 W per light, total of 24 lights, emitting wavelength = 450 ± 20 nm, the irradiation spectrum is shown in Fig. S1 in Supporting information) were used as the light source. The total light intensity was determined by a digital radiodetector (PM100A, THORLABS GmbH, Dachau, Germany) to be approximately 20 mW cm^{-2}. In a typical process, 200 mg of the photocatalyst was dispersed in 50 mL of 0.5 mmol L^{-1} BA acetonitrile solution in a beaker. The suspension was then magnetically stirred in the dark for 1 h to ensure the adsorption-desorption equilibrium. After light illumination, the products were regularly analyzed by a gas chromatograph (GC, GC 5890, China) equipped with a SE-54 GC capillary column (30 m × 0.53 mm, 0.3 μm) and a FID detector. The yield of BAD, the selectivity for BAD, and conversion of BA were calculated using the following equations (Eqs. (1)–(3)):

$$\text{Yield}(\%) = \frac{C_{BAD}}{C_0} \times 100 \tag{1}$$

$$\text{Selectivity}(\%) = \frac{C_{BAD}}{C_0 - C_{BA}} \times 100 \tag{2}$$

$$\text{Conversion}(\%) = \frac{C_0 - C_{BA}}{C_0} \times 100 \tag{3}$$

where C_0 is the initial concentration of BA, C_{BA} and C_{BAD} are the concentrations of BA and BAD at a certain period of time after the photocatalytic reaction, respectively [30].

2.3. Catalyst characterization

The crystal phase composition of samples were determined by a Bruker D8 Advance (Bruker AXS, Germany) powder X-ray diffraction (XRD) using a Cu Kα radiation. The sample's surface composition and valence-band X-ray photoelectron spectroscopy (VB XPS) were obtained by an X-ray photoelectron spectroscopy (XPS, Thermo Scientific ESCALAB 250Xi, USA) with an Al Kα X-ray source. Fourier transform infrared spectroscopy (FT-IR) spectra were performed on a Nexus 470 FT-IR spectrometer (Nicolet, USA) using KBr as a background. The thermo-gravimetric analysis (TGA) was performed using a thermal analyzer (TGA Q500, TA Instruments) with a range of temperature from 30 to 800 °C in air atmosphere.

Morphological characterization was observed by a field emission scanning electron microscope (FE-SEM, S4800, Hitachi). High resolution transmission microscopy (HRTEM) observation was carried out on a field emission transmission electron microscopy (TEM, Tecnai G2 F20, FEI). UV–vis diffuse reflectance spectra (UV–vis DRS) were obtained on a UV 2700 spectrometer (Shimadzu, Japan) using BaSO$_4$ as a reference material and converted from reflection to absorbance by the Kubelka-Munk method. The Brunauer–Emmett–Teller (BET) surface areas were measured by N$_2$ adsorption/desorption measurements (ASAP 2020, Micromeritics, USA) at 77 K. A desorption isotherm was used to determine the pore size distribution using the Barrett-Joyner-Halenda (BJH) method.

The photocurrent measurements were performed on an

electrochemical workstation (CHI-660E, Shanghai Chenhua Apparatus Corporation, China). A 9 W blue LED lamp was used as the light source. A standard three-electrode cell containing a platinum plate as counter electrode, a commercial Ag/AgCl electrode as reference electrode, the as-prepared samples as the working electrodes, and a $0.5 \, mol \, L^{-1}$ Na_2SO_4 aqueous solution as an electrolyte. The photoluminescence (PL) spectra for solid powders were investigated on an Edinburgh FL/FS900 Spectrophotometer (Edinburgh Instruments Ltd, Livingston, UK). The zeta potential (Zetaplus, zeta potential analyzer, Brookhaven Instruments Co.) was used to characterize the surface charge of the as-prepared sample.

Electron paramagnetic resonance (EPR, JES FA-200, JEOL, Japan) measurement was used to detect oxygen vacancies (OV) and bromine vacancies (BrV) at 77 K. The g factor was obtained by taking the signal of manganese as standard. And in situ $\cdot O_2^-$ and $\cdot OH$ radicals producing under light ($\lambda > 450 \, nm$) irradiation were also identified, using 5,5-dimethyl-1-pyrroline-*N*-oxide (DMPO) as a spin trap.

2.4. Computational methods

The Mulliken charge distributions of BA, BA$^-$ (alkoxide anion), and BAD were calculated using the density functional theory (DFT) on the Gaussian 09 program. The optimized geometries were obtained using the B3LYP method based on the $6\text{-}311 + +G(d,p)$ basis set. All optimizations were performed without symmetry restrictions and followed by harmonic frequency analyses to ensure that the optimized conformation was true to the global minimum.

A population analysis of $Bi_{24}O_{31}Br_{10}$ (COD ID: 8104381) was performed with the plane-wave pseudopotential DFT method using the Cambridge serial total energy package (CASTEP) code in Materials Studio, and the Perdew-Burke-Ernzerhof (PBE) generalized gradient approximation (GGA) was used for the exchange-correlation functional. The energies and electronic structures were calculated based on the optimized geometric structures.

3. Results and discussion

3.1. Characterization of photocatalyst

Fig. 1A shows the XRD patterns of the precursor and as-synthesized sample. It can be seen from the results that the crystallinity of the precursor is rather low, and its crystal phase cannot be fully identified. However, after calcination at 450 °C, the diffraction peaks of the as-synthesized sample can be indexed well to monoclinic $Bi_{24}O_{31}Br_{10}$ (JCPDS 75-0888) with a high crystallinity and high purity. The results are completely different from those of our previous study [22], where pure $Bi_4O_5Br_2$ was obtained after a microwave reaction using the same procedure and experimental conditions, except no glucose was added. Besides, compared with the standard card, the diffraction intensity of (30−6) and (40−6) planes of as-synthesized sample is significantly enhanced, meaning that the sample has special growth orientations and is mainly dominated by unusual facets. A typical HRTEM image of as-synthesized sample is shown in Fig. S2 (Supporting information), which clearly reveals it has a lattice spacings of 0.28 nm (corresponding to the (30−6) plane in $Bi_{24}O_{31}Br_{10}$). The results demonstrate that the as-synthesized $Bi_{24}O_{31}Br_{10}$ is well-crystallized with unusual exposed facets, which may bring its special properties and activities.

To determine the role of glucose, an XPS analysis was performed on the samples before and after the calcination, as shown in Fig. 1B–F. The XPS survey spectra (Fig. 1B) revealed two samples containing identical elements of Bi, O, Br, and C. Nevertheless, their high-resolution XPS spectra exhibited marked differences. The core level spectra of Bi 4f (Fig. 1C) and Br 3d (Fig. 1D) in the two samples were similar and can be identified as Bi^{3+} and Br$^-$, respectively [31]. The binding energy (BE) of the calcined sample was slightly higher than that of the precursor, indicating that the electron density around the atoms in the calcined

sample is somewhat increased. Besides, a small amount of Bi° was also found at a BE of 157.2 eV [32] in the sample before the calcination. The O 1s spectra can be divided into two peaks at BE of 530.0 and 531.6 eV (Fig. 1E), which belong to the oxygen atoms in Bi−O and O−H, respectively [33]. However, the peak area of 531.6 eV in the precursor is much larger than that in the calcined sample, which implied that the –OH signal is not simply due to the surface adsorption of water. The C 1s spectra were significantly different for the two samples (Fig. 1F). The sample after calcination had only one peak at BE 284.4 eV, which was attributed to adventitious carbon species (C−C) that originate in the XPS instrument. However, in addition to the peak, the precursor had another two peaks at approximately BE of 286.0 and 287.8 eV, which corresponded to C−O and carbonyl structures, respectively [34]. In addition, XPS quantitative data revealed that the atomic ratios of Br/Bi, O/Bi, and C/Bi in the precursor were 0.523, 3.41, and 3.50, and in the calcined sample were 0.435, 1.04, and 1.01, respectively. As a result, the calcined product was identified as $Bi_{24}O_{31}Br_{10}$, and its precursor is a compound containing Bi (Bi^{3+} and Bi°), Br (Br$^-$), O (Bi−O and O−H), C (C−O and C=O), and H (O−H). The −OH and C-containing groups in the precursor were derived from the glucose (polyhydroxy aldehyde) and its reaction products.

To acquire more evidence, the synthesized samples were further characterized by FT-IR, XRD, and TG techniques. The FT-IR spectra of the samples before and after calcination are presented in Fig. 2G. O−H stretching vibrations were observed at around $3400 \, cm^{-1}$ which is drastically degraded after the calcination. A clear C=O stretch at $1612 \, cm^{-1}$ was examined in the sample before calcination. The other three carbon-based characteristic peaks, including an asymmetrical C−H stretching at $2924 \, cm^{-1}$, a bending vibration of C−H at $1384 \, cm^{-1}$, and a C−O stretching at $1079 \, cm^{-1}$, can be detected in the precursor. These four peaks were significantly reduced after the calcination. On the other hand, a stretch at approximately $540 \, cm^{-1}$ was strengthened after the calcination, which was attributed to the vibration of the Bi−O bonds [35]. Thus, the FTIR results were consistent with the XPS analysis.

To explain the presence of a small amount of Bi° in the precursor, three precursors with different amounts of glucose (3, 6, and 12 mmol) added were synthesized and analyzed by XRD, as depicted in Fig. 1H. The XRD patterns of the three samples were somewhat similar. However, the diffraction peaks of metal bismuth (identified by JCPDS 85-1331) were clearly observed when 12 mmol glucose was added to the system. Although the sample prepared by adding 3 mmol glucose showed no signs of zero-value bismuth, a careful study revealed that characteristic peaks of Bi° could be found in the precursor with 6 mmol glucose. The results illustrated that the presence of Bi° is directly related to the added glucose, and this is possibly because glucose can be used as a reducing agent (presence of −CHO and −OH) to reduce Bi^{3+} to Bi° (E° = 0.308 V) [36].

Thermogravimetric (TG) analysis was used to investigate the calcination process of the precursor. As shown in Fig. 1I, three weight-loss events were observed in the range from room temperature to 800 °C. The weight loss (approximately 2%) before 150 °C is due to the evaporation of moisture in the sample. The weight loss (approximately 10%) between 200 and 400 °C is due to the decomposition of organic structures in the sample. A platform was exhibited from 400 to 500 °C, at which point $Bi_{24}O_{31}Br_{10}$ exists in a stable formation. The last stage is the weight loss above 500 °C, which is attributed to the decomposition of $Bi_{24}O_{31}Br_{10}$ (progressive loss of Br).

According to the above analysis, the formation of $Bi_{24}O_{31}Br_{10}$ can be described as follows. Before the microwave reaction, EG acts as a strong complexing agent for Bi^{3+} to inhibit the hydrolysis of Bi^{3+} and to avoid Bi^{3+} reacting with Br$^-$. When glucose is added to the system, it also contributes to the coordination of Bi^{3+} and is involved in the creation of precipitates. Thus, the product after the microwave reaction is not a simple bismuth oxybromide but a complex compound containing Bi, O, Br, C, and H. In addition, glucose can further act as a
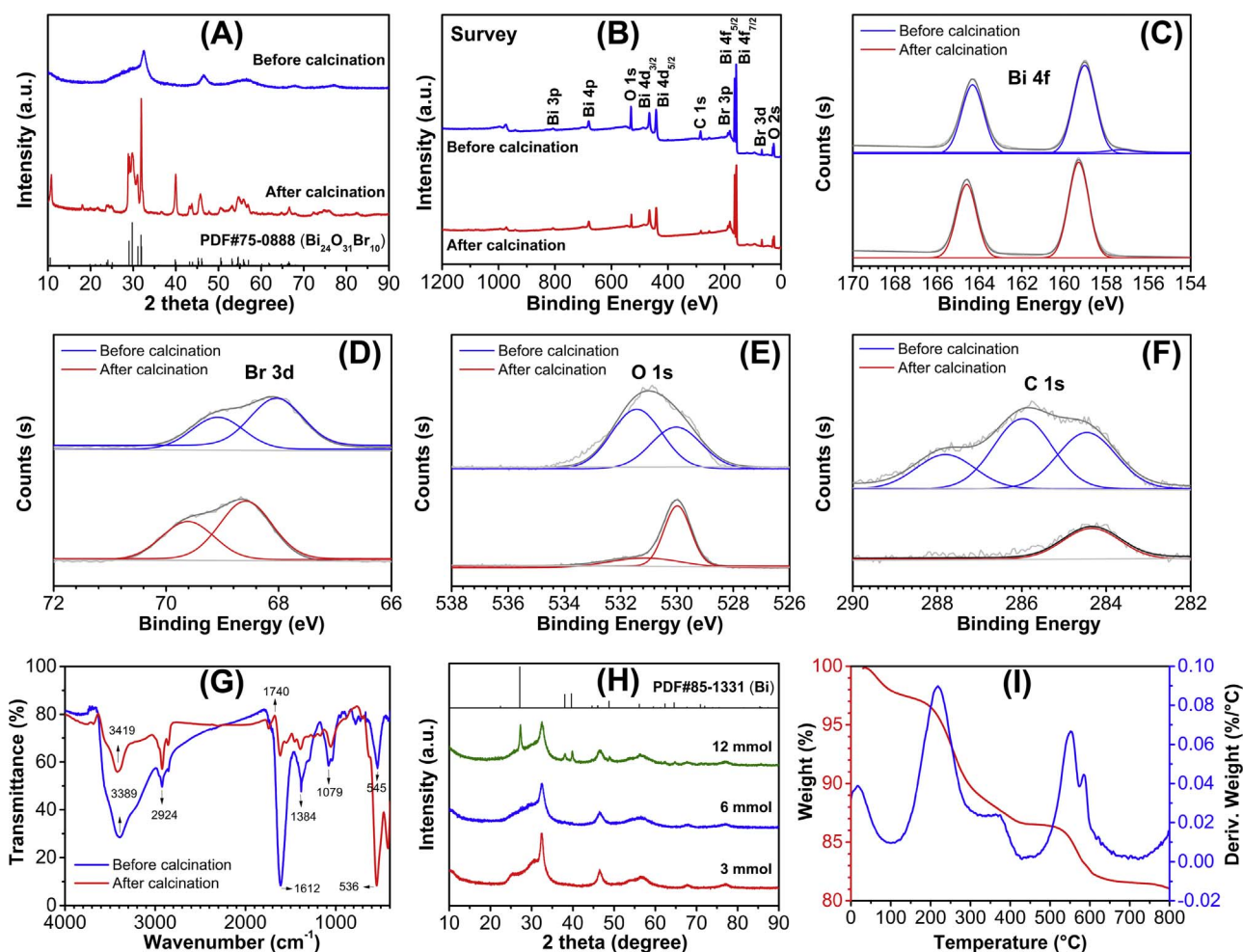
Fig. 1. (A) XRD patterns, (B–F) XPS survey spectra, and (G) FT-IR spectra of the as-synthesized samples before and after calcination; (H) XRD patterns of the samples obtained using varying amounts of glucose; and (I) TG profile of the precursor calcinated under air atmosphere.

reducing agent to reduce Bi^{3+} to $Bi°$. Subsequently, the precursor was calcined in an air atmosphere at 450 °C. The compound first decomposed at approximately 250–450 °C to lose its organic components and transformed into inorganic components. The final product is $Bi_{24}O_{31}Br_{10}$ rather than $Bi_4O_5Br_2$ (although the feed ratio of Bi/Br is 2:1), which is due to the special coordination-calcination process and associated with the partial reduction of Bi^{3+} by glucose, thus that not

all of the Br atoms were used to form the final product after the calcination.

SEM analysis was used to study the morphology and microstructure of the precursor and as-prepared $Bi_{24}O_{31}Br_{10}$, as shown in Fig. 2. It can be observed from Fig. 2A that the precursor presents dispersed 3D flower-like microspheres consisting plenty of nanosheets. The average diameter of the microspheres is approximately 0.6 μm. The thickness of
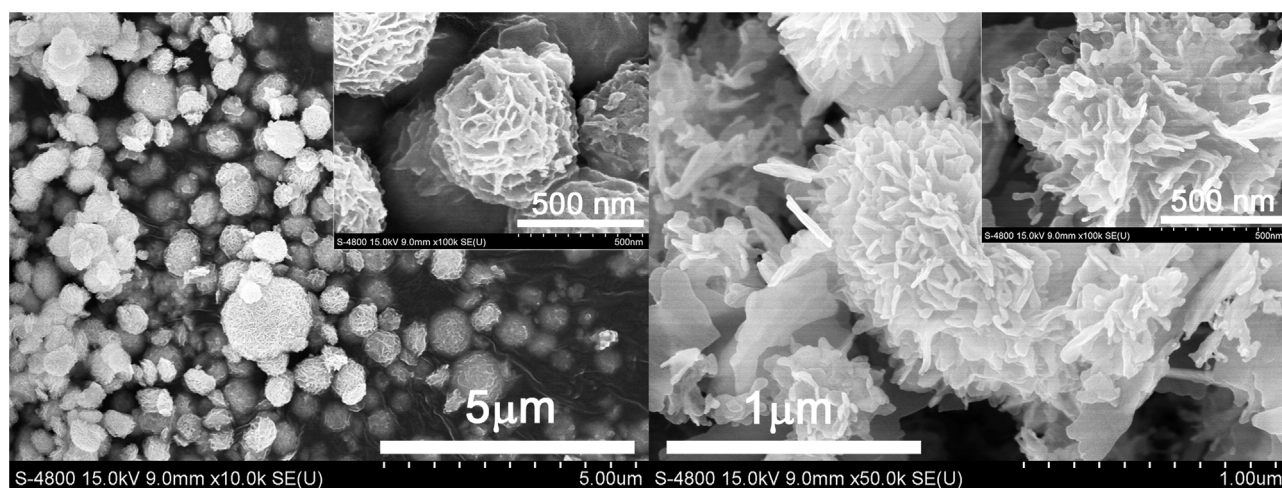
Fig. 2. SEM and high-magnification SEM (inset) images of the synthesized sample before and after calcination.
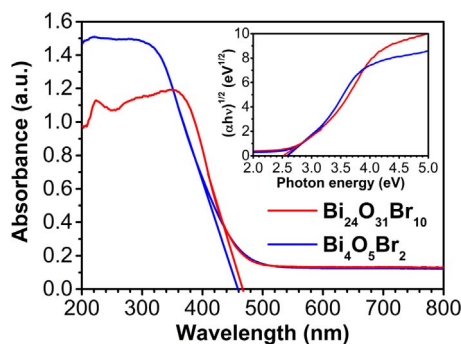
Fig. 3. UV–vis diffuse reflection spectra of the synthesized $Bi_{24}O_{31}Br_{10}$ and $Bi_4O_5Br_2$; inset displays plots of $(\alpha h\nu)^{1/2}$ vs. photon energy ($h\nu$).

Fig. 4. Nitrogen adsorption–desorption isotherms and corresponding pore size distribution plots (inset) for the synthesized $Bi_{24}O_{31}Br_{10}$ and $Bi_4O_5Br_2$.

the nanosheets was approximately 8 nm according to a high-magnification SEM image (inset of Fig. 2A). Interestingly, although the reaction process and other conditions are similar, the addition of glucose leads to significant differences in the product morphology compared to that of the previous reported sample ($Bi_4O_5Br_2$ with aggregated nanoflakes) [22], revealing that glucose may also act as a structure-directing agent in this process. The SEM images of the as-synthesized $Bi_{24}O_{31}Br_{10}$ are shown in Fig. 2B. Compared to its precursor, the calcination product mostly retained flower-like structures composed of nanosheets, but some microspheres were destroyed. And the nanosheet thickness slightly increased (~ 10 nm) according to a high-resolution SEM image (inset of Fig. 2B). Recently, the development of 3D hierarchical catalysts has attracted great interest for enhance the catalytic activity since their contain benefits such as high surface area, high surface-to-volume ratio, anti-aggregation ability, abundant transport paths for organic molecules, and good recyclability [37–41]. Thus, the 3D flower-like $Bi_{24}O_{31}Br_{10}$ may has a better catalytic performance.

The energy band structures and optical properties of a semiconductor are considered key factors in its photocatalytic activity. Fig. 3 shows the UV-vis diffuse reflectance spectroscopy (DRS) of the as-synthesized $Bi_{24}O_{31}Br_{10}$ and $Bi_4O_5Br_2$. It was clearly observed that the optical absorption edges of $Bi_{24}O_{31}Br_{10}$ and $Bi_4O_5Br_2$ were 467 and 459 nm, respectively, which implied that these two semiconductors can respond well to visible light and blue LED light ($\lambda = 450 \pm 20$ nm) irradiation. The band gap energies (E_g) of the two samples were estimated using the Kubelka-Munk function (Eq. (4)) [42]:

$$\alpha(h\nu) = A(h\nu - E_g)^{n/2} \tag{4}$$

where α is the adsorption coefficient, h is the Planck constant, ν is the incident light frequency, A is an energy-independent constant, and n is 4 for their indirect transitions [43]. Accordingly, the E_g of $Bi_{24}O_{31}Br_{10}$ and $Bi_4O_5Br_2$ can be calculated from a plot of $(\alpha h\nu)^{1/2}$ versus $h\nu$. As shown in the inset of Fig. 3, the band gap energy of $Bi_{24}O_{31}Br_{10}$ is estimated to be 2.51 eV, which is slightly lower than that of $Bi_4O_5Br_2$ (2.59 eV). The Eg values acquired here is close to that in previous report [27]. In addition, the band position of the synthesized $Bi_{24}O_{31}Br_{10}$ can be further evaluated using the following empirical equation (Eqs. (5) and (6)) [44]:

$$E_{VB} = X - E^e + 0.5E_g \tag{5}$$

$$E_{CB} = E_{VB} - E_g \tag{6}$$

where E_{VB} and E_{CB} are the VB and conduction band (CB) edge potentials for the semiconductor, respectively, X is the electronegativity computed from the geometric mean of the electronegativities for the constituent atoms, and E^e is the energy of the free electrons on the hydrogen scale (4.5 eV). Then, the E_{VB} and E_{CB} potentials of the photocatalyst can ultimately be evaluated using the following equation (Eq. (7)) to reflect the effect of pH [45]:
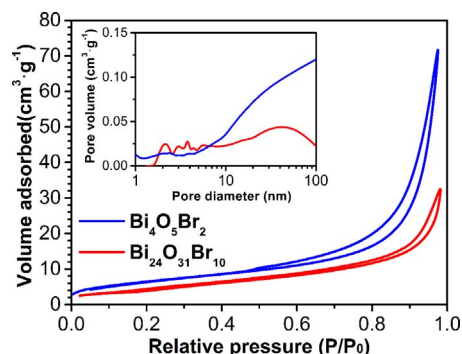
$$E = E^0 - 0.05915 \times pH \tag{7}$$

Accordingly, the E_{CB} and E_{VB} values of the as-synthesized $Bi_{24}O_{31}Br_{10}$ were estimated to be -0.13 and 2.38 V, respectively, at pH 7. To further confirm the energy band structures of the catalyst, the total densities of VB states of the as-synthesized $Bi_{24}O_{31}Br_{10}$ was measured by VB XPS. As shown in Fig. S3 (Supporting information), the VB top of sample was determined to be 2.39 eV, which is almost identical as the calculated value using the empirical formulas. Thus, the VB potential of $Bi_{24}O_{31}Br_{10}$ is higher than the redox potential of BA/BAD (~ 1.98 V), but it is below the potentials of BAD/oxidized BAD (~ 2.50 V) [19], suggesting that the photocatalyst may exhibit good selectivity for the photocatalytic conversion of BA into BAD from a thermodynamic perspective.

N_2 adsorption-desorption isotherms were measured to evaluate the surface area and pore size distribution of the synthesized $Bi_{24}O_{31}Br_{10}$ and $Bi_4O_5Br_2$. As shown in Fig. 4, both samples exhibit type-IV adsorption isotherms with an H3 hysteresis loop, indicating their mesoporous structures according to the IUPAC classification criteria [46]. The BET specific surface area of $Bi_{24}O_{31}Br_{10}$ was measured to be 16.34 $m^2 g^{-1}$, which is lower than that of $Bi_4O_5Br_2$ sample (23.86 $m^2 g^{-1}$). The pore size distributions of $Bi_{24}O_{31}Br_{10}$ and $Bi_4O_5Br_2$ are also shown in the inset of Fig. 4, and their average pore diameters were obtained using the BJH method to be 12.86 and 21.76 nm, respectively. The pores with widely distributed in $Bi_{24}O_{31}Br_{10}$ may be produced by the interspaces between the nanosheets and microspheres, which is consistent with the SEM observations.

3.2. Photocatalytic oxidation of BA

The photocatalytic performance of the as-synthesized $Bi_{24}O_{31}Br_{10}$ was evaluated for the photocatalytic oxidation of BA into BAD under blue LED irradiation and compared to reported typical catalysts, including $Bi_4O_5Br_2$ [22], $Bi_{12}O_{17}Cl_2$ [19], and nano-TiO_2 (which has displayed a > 99% conversion and > 99% selectivity for the oxidation of BA into BAD under visible light due to the formation of a visible-light-sensitized surface complex) [11]. As shown in Fig. 5A, when using $Bi_{24}O_{31}Br_{10}$ as a photocatalyst, the concentration of BA declined rapidly, and the concentration of BAD (oxidized product) increased with the reaction evolution time. After reaction for 120 min, a 92.5% conversion and > 99% selectivity were reached. If the reaction time was prolonged to 150 min, both the conversion ratio and the selectivity reached > 99%. Under identical experimental conditions, the conversion and selectivity over $Bi_4O_5Br_2$ were 57.2% and 99.2%, 11% and 96.8% over $Bi_{12}O_{17}Cl_2$, and 61.1% and 97.8% over TiO_2, respectively. Hence, the as-synthesized 3D flower-like $Bi_{24}O_{31}Br_{10}$ exhibited a superb photocatalytic conversion efficiency and selectivity for the aerobic oxidation of BA into BAD under blue LED irradiation at ambient conditions.

The conversion kinetics of BA over the as-synthesized $Bi_{24}O_{31}Br_{10}$, TiO_2, $Bi_4O_5Br_2$, and $Bi_{12}O_{17}Cl_2$ were examined by fitting the experimental data to pseudo-first order kinetics according to the Langmuir-

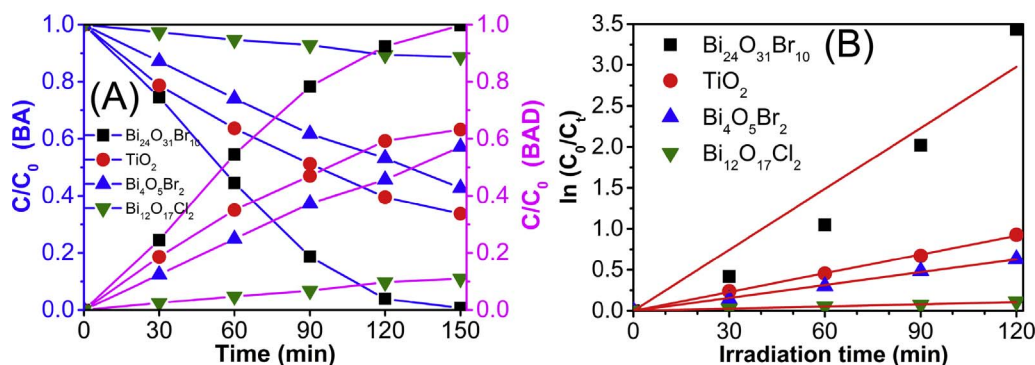Fig. 5. (A) Photocatalytic oxidation of BA into BAD over the synthesized $Bi_{24}O_{31}Br_{10}$, $Bi_4O_5Br_2$, $Bi_{12}O_{17}Cl_2$, and TiO_2 under blue LED irradiation. (B) Linear plots of $\ln(C_0/C_t)$ versus the reaction time.

Hinshelwood model (Eq. (8)) [47]:

$$-\ln\left(\frac{C_t}{C_0}\right) = k \cdot t \tag{8}$$

where C_0 is the initial concentration of BA, C_t is the concentration of BA at a certain reaction time, and k (min^{-1}) is the apparent reaction rate constant defined by plotting $\ln(C_0/C_t)$ vs. the reaction time (t). As shown in Fig. 5B, the k values for $Bi_{24}O_{31}Br_{10}$, TiO_2, $Bi_4O_5Br_2$, and $Bi_{12}O_{17}Cl_2$ were calculated to be 0.0248, 0.00763, 0.00523, and 0.000890 min^{-1}, respectively. Thus, the reaction rate over $Bi_{24}O_{31}Br_{10}$ was 3.3-, 4.7-, and 27.8-fold higher than that over nano-TiO_2, $Bi_4O_5Br_2$, and $Bi_{12}O_{17}Cl_2$, respectively.

For further evaluation, six $Bi_{24}O_{31}Br_{10}$ samples (labeled as S2–S7) were prepared using various techniques in the literatures [24–29] and tested under the same conditions. As shown in Fig. 6A, all the $Bi_{24}O_{31}Br_{10}$ samples exhibited photocatalytic activities with excellent selectivity, which indicated that the energy band structure of $Bi_{24}O_{31}Br_{10}$ is a key factor in determining its selectivity, and the synthesis methods significantly influenced their photocatalytic activities. Among them, the $Bi_{24}O_{31}Br_{10}$ synthesized in this work showed the highest efficiency. Additionally, the other two samples with 3 or 12 mmol glucose were also prepared by the same process to test the influence of the amount of glucose on the photocatalytic performance. As shown in Fig. 6B, the results revealed that they all presented decent photocatalytic activities, but none of the actives were higher than that of 6 mmol sample, suggesting that the amount of glucose may affect the structure of the final product and 6 mmol of glucose is the optimal condition.

In order to measure the catalytic performance of as-synthesized $Bi_{24}O_{31}Br_{10}$ at high BA concentration, an additional experiment was carried out using a 20-fold initial concentration of BA (10 mmol L^{-1}) while keep other conditions unchanged. As shown in Fig. S4 (Supporting information), after 24 h of photocatalytic reaction, BA is completely converted with good selectivity. To study the effect of 3D structures on the photocatalytic activity, the as-synthesized flower-like $Bi_{24}O_{31}Br_{10}$ was treated firstly by an ultrasonic cell crushing device for 1 h to break down the structures, then a comparative experiment was

performed. The results revealed that the sonicated sample did not display a significant reduction in performance (about 9% reduction after 150 min of photoreaction). The results indicate that the 3D structure of sample does not play a critical role in this system.

Stability and recyclability are important features for a catalyst in practical use. To examine the recyclability of the as-synthesized $Bi_{24}O_{31}Br_{10}$, sample powders were recovered and used another three times under the same conditions. As shown in Fig. 7A, the conversion efficiency and selectivity of the $Bi_{24}O_{31}Br_{10}$ samples were almost constant over the four cycles, inferring excellent recyclability. In addition, the XRD patterns of the samples before or after the recycling experiments (Fig. 7B) remains intact, which indicates that the as-synthesized $Bi_{24}O_{31}Br_{10}$ has a high chemical and photo stability. What's more, the SEM images and BET measurement of the recycled sample were also given in Figs. S5 and S6 (Supporting information), respectively, which reveals a high stability of as-synthesized sample. Thus, the $Bi_{24}O_{31}Br_{10}$ sample has a good durability with highly effective for the conversion of BA into BAD, which makes it promising for practical applications.

3.3. Reaction mechanism

Compared to typical reported high-activity catalysts such as $Bi_4O_5Br_2$, $Bi_{12}O_{17}Cl_2$, and nano-TiO_2 (Fig. 5), or $Bi_{24}O_{31}Br_{10}$ samples prepared by other methods (Fig. 6A), the as-synthesized $Bi_{24}O_{31}Br_{10}$ presented a superior photocatalytic activity for the conversion of BA to BAD. However, the sample does not appear advantageous in terms of specific surface area (Fig. 4) or light absorption (Fig. 3), which means that its photocatalytic activity may be related to the essential structure of $Bi_{24}O_{31}Br_{10}$ and other beneficial characteristics obtained by the synthetic process.

To help understand the photocatalytic performance of the synthesized $Bi_{24}O_{31}Br_{10}$, photoelectrochemical experiments were used to study the photogenerated electron transfer over the catalyst under blue LED illumination, which may directly reflect the separation of photogenerated carriers. The photocurrent-time curves of $Bi_{24}O_{31}Br_{10}$ and $Bi_4O_5Br_2$ photoelectrodes over five on-off cycles were recorded, as shown in Fig. 8A. The results revealed that $Bi_{24}O_{31}Br_{10}$ holds

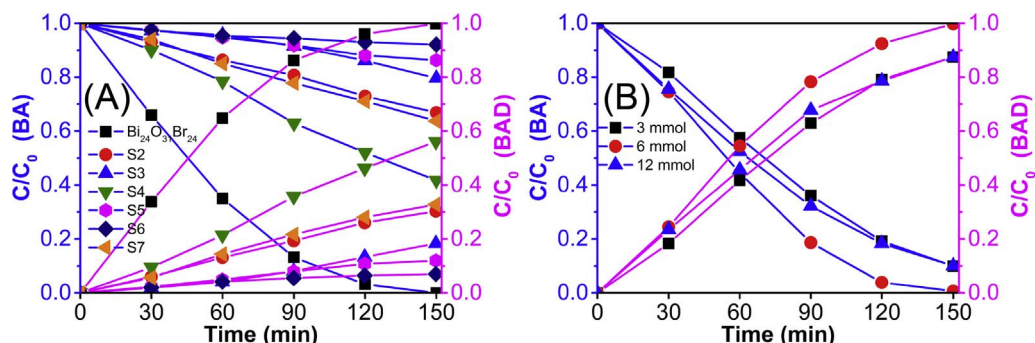Fig. 6. (A) Photocatalytic BA/BAD conversion activity over the synthesized $Bi_{24}O_{31}Br_{10}$ and six $Bi_{24}O_{31}Br_{10}$ samples prepared by different methods; (B) the effect of the glucose content on the photocatalytic BA/BAD conversion.

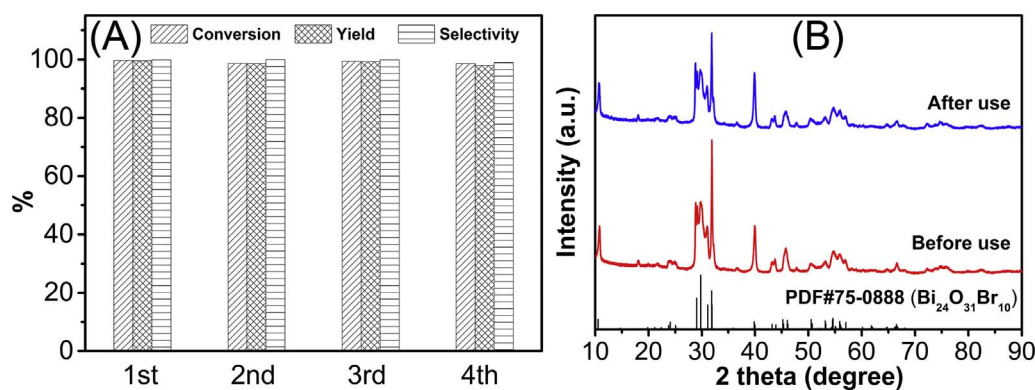approximately six times more photocurrent than $Bi_4O_5Br_2$ under identical conditions. In addition, the room-temperature photoluminescence (PL) spectra of the $Bi_{24}O_{31}Br_{10}$ and $Bi_4O_5Br_2$ samples (Fig. 8B) show that both samples exhibit an emission peak at wavelength approximately 600 nm owing to the combination of photogenerated electron-hole pairs. The PL intensity of $Bi_{24}O_{31}Br_{10}$ is much weaker than that of $Bi_4O_5Br_2$, indicating that the former exhibits a lower recombination rate of electrons and holes [48].

The separation efficiency of the photogenerated charges may strongly relate to the photocatalyst structure. EPR measurements were used to detect possible defects in the synthesized $Bi_{24}O_{31}Br_{10}$. As shown in Fig. 8C and D, a strong EPR signal at g = 2.004 is attributed to the presence of oxygen vacancies (OV) [24], and a noticeable signal for bromine vacancies (BrV) was also found at 323.3 mT [49]. OV and BrV may trap electrons for their positive charge and prolong the lifetime of the photogenerated holes [50]. Thus, the as-synthesized $Bi_{24}O_{31}Br_{10}$ retains both OV and BrV would enhance the separation of photogenerated carriers and bring to a superior photocatalytic performance.

To reveal the roles of the primary active oxygen species during the photocatalytic transformation of BA over the $Bi_{24}O_{31}Br_{10}$ catalyst, radical trapping experiments were performed by adding a series of
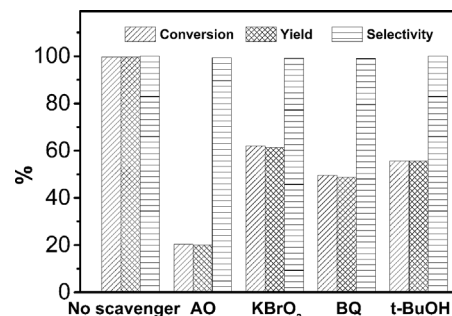

Fig. 9. Photocatalytic conversion of BA into BAD over the synthesized $Bi_{24}O_{31}Br_{10}$ with various radical scavengers under blue LED irradiation for 150 min: No scavenger, AO, $KBrO_3$, BQ, and t-BuOH.

scavengers to the system: Ammonium oxalate (AO) was used to quench h^+; $KBrO_3$ was added to eliminate photogenerated e^-; benzoquinone (BQ) was introduced to scavenge $\cdot O_2^-$; and tertiary butanol (t-BuOH) was used as a scavenger of $\cdot OH$. The results (Fig. 9) show that the selectivity in all the tests was > 99%, revealing the selectivity of the photocatalytic BA/BAD conversion is only a thermodynamic concern
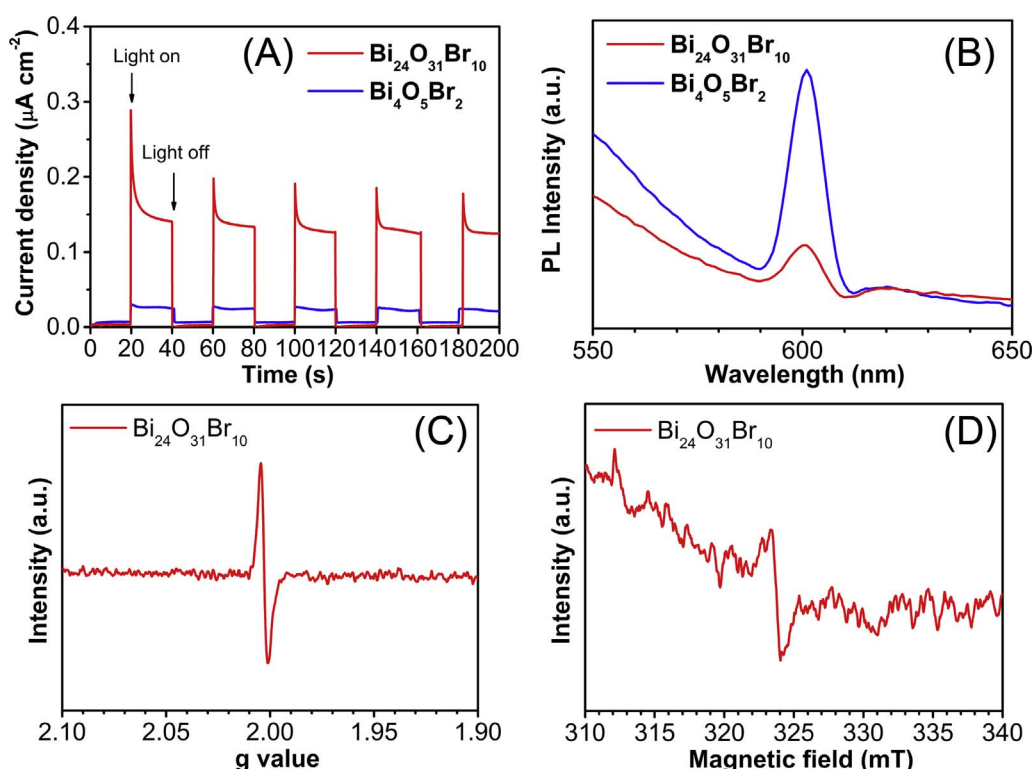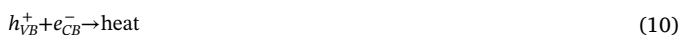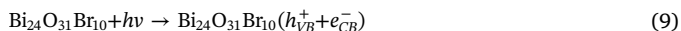

Fig. 8. (A) Transient photocurrents of the synthesized $Bi_{24}O_{31}Br_{10}$ and $Bi_4O_5Br_2$ photoelectrodes under blue LED light irradiation; (B) Photoluminescence spectra of the synthesized $Bi_{24}O_{31}Br_{10}$ and $Bi_4O_5Br_2$ samples; and EPR signals of the oxygen vacancies (C) and bromine vacancies (D) over the synthesized $Bi_{24}O_{31}Br_{10}$.

associated with the band structure of the photocatalyst. However, the conversion rates of BA confirm different degrees of inhibition after the addition of these scavengers. When AO was added, the conversion drastically decreased, which suggested that the photogenerated holes play key roles in the system. In addition, after the addition of $KBrO_3$ and BQ, the photocatalytic activities also notably declined, suggesting that the photogenerated electrons and $\cdot O_2^-$ are likely to be involved in the process. It is well known that superoxide radicals ($\cdot O_2^-$) can form through the reaction of oxygen molecules with electrons which potential is more negative than the standard redox potential of $O_2/\cdot O_2^-$ (-0.33 V vs. NHE). In this case, the relatively positive CB potential of $Bi_{24}O_{31}Br_{10}$ (-0.13 V vs. NHE) appears to be unfavorable for reactions with O_2. However, under blue LED irradiation (E = 2.76 ± 0.12 eV), some electrons on the VB bands of $Bi_{24}O_{31}Br_{10}$ (+2.38 V) can be excited to a higher energy state (up to -0.5 V), which could possibly trap the dissolved oxygen to produce $\cdot O_2^-$.

Unexpectedly, when t-BuOH was added to scavenge $\cdot OH$, the conversion rate also decreased, which indicated that $\cdot OH$ may be involved in the reaction, in contrast to previous reports using $Bi_4O_5Br_2$ as a catalyst [22]. It is well known that since the standard redox potential of Bi^{5+}/Bi^{3+} (E° = 1.59 V) is smaller than that of $\cdot HO/OH^-$ (E° = 1.99 V) [18], bismuth-based photocatalysts generally cannot generate $\cdot OH$ under visible-light irradiation. To reveal the formation of hydroxyl radicals, in situ EPR was performed using DMPO spin-trapping under light irradiation. As shown in Fig. 10A, the signals of DMPO-$\cdot O_2$-adducts developed over the irradiation time. Unlike the fast production of $\cdot O_2^-$, no peaks for $\cdot OH$ were detected before the exposure time reached 8 min (Fig. 10B), but strong $\cdot OH$ signals were observed after continued irradiation. This suggests that $\cdot OH$ may not be directly produced but is instead derived from $\cdot O_2^-$. Compared to $Bi_4O_5Br_2$ [22], under identical conditions, more $\cdot O_2^-$ was generated on $Bi_{24}O_{31}Br_{10}$ due to the presence of OV and BrV (Fig. 8C and D), and these surface defects can easily capture photogenerated e^- and non-polar molecules O_2 that react with each other to generate $\cdot O_2^-$ [51]. Then, $\cdot O_2^-$ further reacted with H^+ to produce $\cdot OH$. The process can be depicted by the following reactions (Eqs. (9)–(14)):

$$Bi_{24}O_{31}Br_{10} + h\nu \rightarrow Bi_{24}O_{31}Br_{10}(h_{VB}^+ + e_{CB}^-) \tag{9}$$

$$h_{VB}^+ + e_{CB}^- \rightarrow heat \tag{10}$$

$$e_{CB}^- + O_2 \rightarrow \cdot O_2^- \tag{11}$$

$$\cdot O_2^- + H^+ \rightarrow \cdot OOH \tag{12}$$

$$\cdot O_2^- + \cdot OOH + H^+ \rightarrow H_2O_2 + O_2 \tag{13}$$

$$H_2O_2 + e_{CB}^- \rightarrow \cdot OH + OH^- \tag{14}$$

To investigate the mechanism of selective oxidation of BA into BAD, the reaction pathway by which BA loses two H atoms from its structure must be determined. By using an ^{18}O isotope labeling technique, Zhang

et al. proposed a two-step dehydrogenation route [17,19], where BA firstly deprotonates and is then oxidized by photogenerated h^+, while O_2 and its derivatives do not contribute to the construction of BAD, which seems reasonable. To verify the mechanism and clarify the interaction between the reactants and products with $Bi_{24}O_{31}Br_{10}$, the charge distribution of the atoms in BA, BA$^-$, BAD, and the $Bi_{24}O_{31}Br_{10}$ crystal were computed by quantum chemistry methods, as shown in Fig. 11 and Table 1. It is generally agreed that the reactants must bond with the catalyst to form an intermediate at the beginning of a catalytic reaction. According the results, if BA is the reactant (Fig. 11A and Table 1), bonding must occur on Bi^{3+} in $Bi_{24}O_{31}Br_{10}$ and C atoms in BA molecules since the charges of some C atoms in BA are more negative than that on O atom. However, if BA loses a proton to form BA$^-$ (alkoxide anion), the results (Fig. 11B and Table 1) show that the charge of the O atom is the most negative, and thus, Bi^{3+} can interact with O^{2-} in BA$^-$. At this stage, if the photogenerated h^+ on the surface of $Bi_{24}O_{31}Br_{10}$ can snatch an electron from the O atom (rich in electronics, without interference of hydrogen), its structure will rearrange and lose a proton to form BAD. Once the production of BAD, as the charge on the C atoms in BAD is more negative than that on the O atom (Fig. 11C and Table 1), BAD does not easily to bond with $Bi_{24}O_{31}Br_{10}$ and tend to separate from the catalyst surface, preventing the possibility of further oxidation. Besides, the zeta potential measurement (Fig. S7, Supporting information) showed that the surface charge of the as-synthesized $Bi_{24}O_{31}Br_{10}$ is positive, which favors the adsorption of anions (BA$^-$) rather than BA and BAD on its surface.

Based on the above analysis, a possible reaction mechanism for the photocatalytic selective oxidation of BA into BAD over the as-synthesized $Bi_{24}O_{31}Br_{10}$ is suggested in Scheme 1. First, BA deprotonates to generate BA$^-$ and H^+. Since $Bi_{24}O_{31}Br_{10}$ exhibits a positive charge surface, BA$^-$ is easily adsorbed on the surface of the catalyst and bonds O^{2-} with Bi^{3+} to form an intermediate. By reacting with the photogenerated h^+, losing an electron, and rearranging, the intermediate transforms into BAD and separates from the photocatalyst surface because of the relatively small polarity of BAD. Thanks to the presence of surface defects (OV and BrV) on the as-synthesized $Bi_{24}O_{31}Br_{10}$, it can trap photogenerated e^- and dissolved O_2 easily to extend the lifetime of the photogenerated carriers and produce $\cdot O_2$-, which further reacts with H^+ to produce $\cdot OH$. Although both $\cdot O_2$- and $\cdot OH$ may likely to react with BA or BA-, according to the experimental results (> 99% selectivity in all tests), these two active species do not appear to be involved in the formation of BAD but act as consuming agents of H^+ to further improve the photocatalytic efficiency and release H_2O. Thus, due to the proper band structures and excellent surface properties of the as-synthesized $Bi_{24}O_{31}Br_{10}$, a high selectivity and high conversion for the photocatalytic transformation of BA/BAD is achieved.

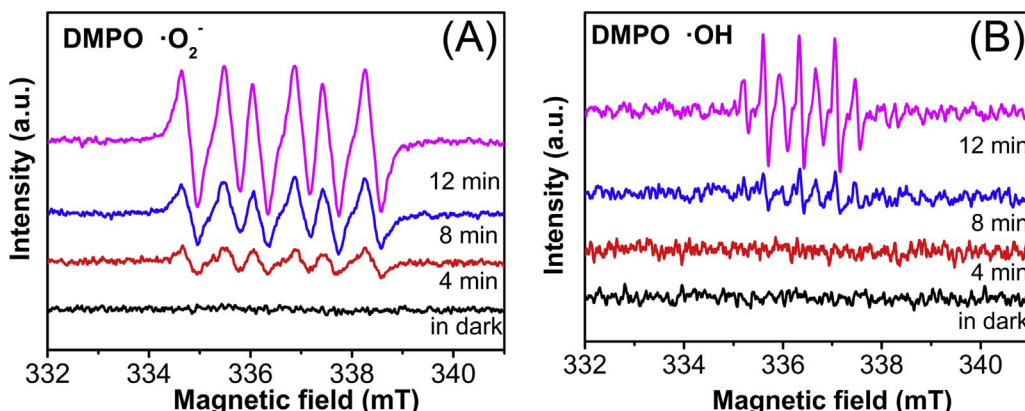**Fig. 10.** (A and B) DMPO spin-trapping EPR spectra for DMPO-$\cdot O_2^-$ and DMPO-$\cdot OH$ over $Bi_{24}O_{31}Br_{10}$ under visible-light ($\lambda > 450$ nm) irradiation.
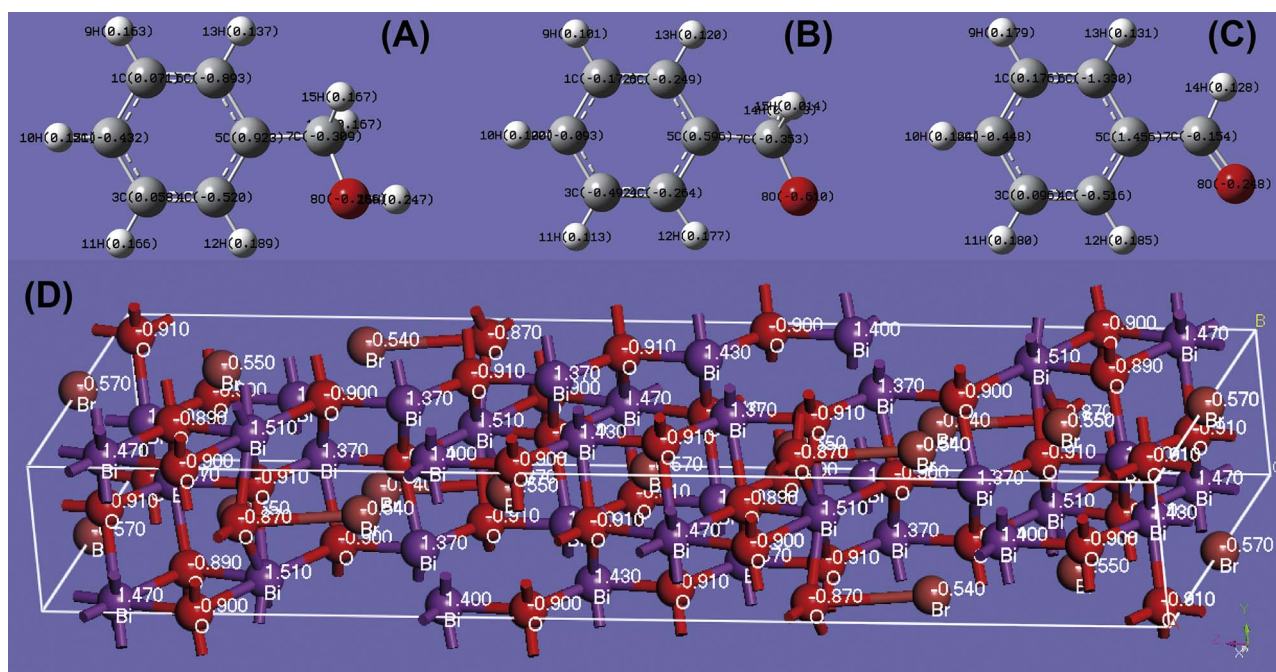
Fig. 11. Molecular structures and Mulliken charge distributions of (A) BA, (B) BA$^-$, and (C) BAD with the atoms labeled; and (D) Population analysis (Mulliken atomic charges) of the Bi$_{24}$O$_{31}$Br$_{10}$ optimized supercells.

Table 1
Calculation results of Mulliken charge distributions of BA, BA$^-$, and BAD.

Atom	BA	BA$^-$	BAD
C1	0.071	−0.172	0.176
C2	−0.432	−0.093	−0.448
C3	0.058	−0.492	0.096
C4	−0.520	−0.264	−0.516
C5	0.923	0.596	1.456
C6	−0.893	−0.249	−1.330
C7	−0.309	−0.353	−0.153
O8	−0.286	−0.610	−0.248

proper band structure with a VB potential of + 2.38 V, effective separation of photogenerated carriers, surface defects, a positively charged surface, good light absorption, specially exposed facets, and 3D micro/nano-structures, resulting in its outstanding photocatalytic efficiency (> 99%) and selectivity (> 99%) for the conversion of BA into BAD under blue LED irradiation. A direct hole-oxidative and two-step dehydrogenation pathway was proposed based on the experimental results and quantum chemical calculations. The as-synthesized Bi$_{24}$O$_{31}$Br$_{10}$ shows a high stability and recyclability, indicating its potential for practical applications.
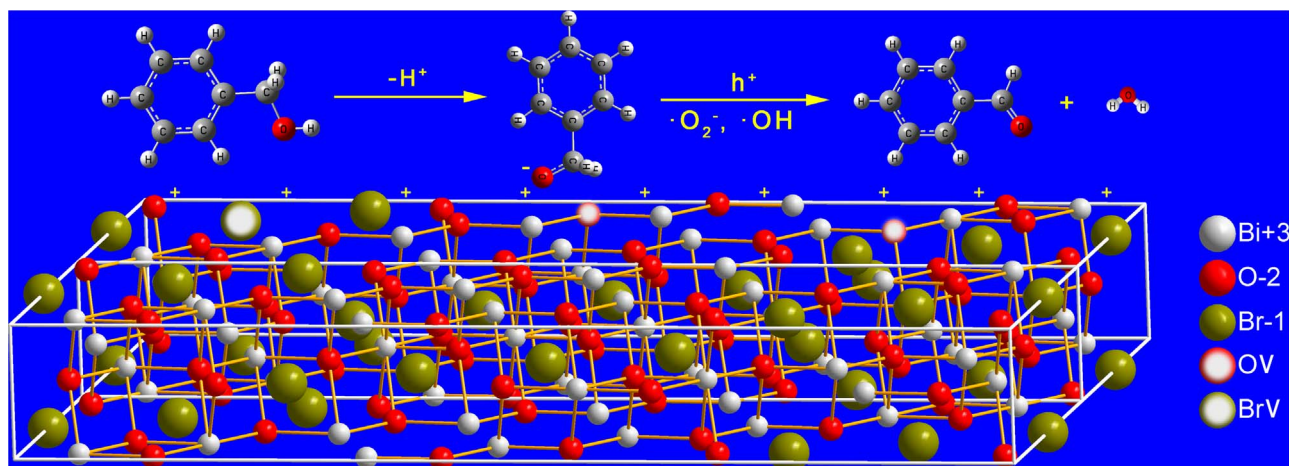
4. Conclusion

In summary, a 3D flower-like Bi$_{24}$O$_{31}$Br$_{10}$ was firstly synthesized through a microwave-calcination route. Glucose plays a key role in the formation of deficient Bi$_{24}$O$_{31}$Br$_{10}$ by acting as a complexing, reducing, and structure-directing agent. The as-synthesized Bi$_{24}$O$_{31}$Br$_{10}$ has a

Scheme 1. Proposed mechanism for the selective photocatalytic oxidation of BA into BAD over deficient Bi$_{24}$O$_{31}$Br$_{10}$ under blue LED irradiation.

Appendix A. Supplementary data

Supplementary material related to this article can be found, in the online version, at doi:https://doi.org/10.1016/j.apcatb.2018.01.076.

References

[1] A. Fujishima, K. Honda, Nature 238 (1972) 37–38.
[2] P.V. Kamat, J. Phys. Chem. C 111 (2007) 2834–2860.
[3] M.R. Hoffmann, S.T. Martin, W.Y. Choi, D.W. Bahnemann, Chem. Rev. 95 (1995) 69–96.
[4] M. Xing, B. Qiu, M. Du, Q. Zhu, L. Wang, J. Zhang, Adv. Funct. Mater. 27 (2017) 1702624.
[5] M. Xing, J. Zhang, B. Qiu, B. Tian, M. Anpo, M. Che, Small 11 (2015) 1920–1929.
[6] R. Zhang, M. Shao, Z. Li, F. Ning, M. Wei, D.G. Evans, X. Duan, Chemistry 23 (2017) 8142–8147.
[7] A. Magdziarz, J.C. Colmenares, O. Chernyayeva, D. Lisovytskiy, J. Grzonka, K. Kurzydlowski, K. Freindl, J. Korecki, Ultrason. Sonochem. 38 (2017) 189–196.
[8] Y. Su, Z. Han, L. Zhang, W. Wang, M. Duan, X. Li, Y. Zheng, Y. Wang, X. Lei, Appl. Catal. B: Environ. 217 (2017) 108–114.
[9] V.R. Choudhary, P.A. Chaudhari, V.S. Narkhede, Catal. Commun. 4 (2003) 171–175.
[10] M.J. Lima, A.M.T. Silva, C.G. Silva, J.L. Faria, J. Catal. 353 (2017) 44–53.
[11] S. Higashimoto, N. Kitao, N. Yoshida, T. Sakura, M. Azuma, H. Ohue, Y. Sakata, J. Catal. 266 (2009) 279–285.
[12] F. Su, S.C. Mathew, G. Lipner, X. Fu, M. Antonietti, S. Blechert, X. Wang, J. Am. Chem. Soc. 132 (2010) 16299–16301.
[13] Y. Liu, P. Zhang, B.Z. Tian, J.L. Zhang, A.C.S. Appl, Mater. Interfaces 7 (2015) 13849–13858.
[14] J. Wan, X. Du, E. Liu, Y. Hu, J. Fan, X. Hu, J. Catal. 345 (2017) 281–294.
[15] Y. Zhang, Y. Xu, RSC Adv. 4 (2014) 2904–2910.
[16] B. Zhang, J. Li, Y. Gao, R. Chong, Z. Wang, L. Guo, X. Zhang, C. Li, J. Catal. 345 (2017) 96–103.
[17] H. Li, F. Qin, Z. Yang, X. Cui, J. Wang, L. Zhang, J. Am. Chem. Soc. 139 (2017) 3513–3521.
[18] X. Xiao, C. Liu, R. Hu, X. Zuo, J. Nan, L. Li, L. Wang, J. Mater. Chem. 22 (2012) 22840–22843.
[19] X. Xiao, J. Jiang, L. Zhang, Appl. Catal. B: Environ. 142–143 (2013) 487–493.
[20] L.Y. Ding, H. Chen, Q.Q. Wang, T.F. Zhou, Q.Q. Jiang, Y.H. Yuan, J.L. Li, J.C. Hu, Chem. Commun. 52 (2016) 994–997.
[21] X.Y. Liu, Y.G. Su, Q.H. Zhao, C.F. Du, Z.L. Liu, Sci. Rep. 6 (2016) 28689.
[22] C. Zheng, G. He, X. Xiao, M. Lu, H. Zhong, X. Zuo, J. Nan, Appl. Catal. B: Environ. 205 (2017) 201–210.
[23] M. Yuan, F. Tian, G. Li, H. Zhao, Y. Liu, R. Chen, Ind. Eng. Chem. Res. 56 (2017) 5935–5943.
[24] F. Li, Q. Wang, J. Ran, Y. Hao, X. Wang, D. Zhao, S.Z. Qiao, Nanoscale 7 (2015) 1116–1126.
[25] Z. Liu, H. Ran, J. Niu, P. Feng, Y. Zhu, J. Colloid Interface Sci. 431 (2014) 187–193.
[26] J. Shang, W. Hao, X. Lv, T. Wang, X. Wang, Y. Du, S. Dou, T. Xie, D. Wang, J. Wang, ACS Catal. 4 (2014) 954–961.
[27] X. Xiao, R. Hu, C. Liu, C. Xing, X. Zuo, J. Nan, L. Wang, Chem. Eng. J. 225 (2013) 790–797.
[28] C. Yu, W. Zhou, J. Yu, F. Cao, X. Li, Chin. J. Chem. 30 (2012) 721–726.
[29] H. Deng, J. Wang, Q. Peng, X. Wang, Y. Li, Chem. Eur. J. 11 (2005) 6519–6524.
[30] S. Meng, X. Ye, X. Ning, M. Xie, X. Fu, S. Chen, Appl. Catal. B: Environ. 182 (2016) 356–368.
[31] H. Cheng, B. Huang, P. Wang, Z. Wang, Z. Lou, J. Wang, X. Qin, X. Zhang, Y. Dai, Chem. Commun. 47 (2011) 7054–7056.
[32] B.I. Podlovchenko, Y.M. Maksimov, S.A. Evlashin, T.D. Gladysheva, K.I. Maslakov, V.A. Krivchenko, J. Electroanal. Chem. 743 (2015) 93–98.
[33] R. Song, H. Jiang, T. Liu, X. Liu, G. Meng, Mater. Res. Bull. 42 (2007) 334–344.
[34] E.T. Kang, H.C. Ti, K.G. Neoh, T.C. Tan, Polym. J. 20 (1988) 399–406.
[35] C. Wang, C. Shao, Y. Liu, L. Zhang, Scripta Mater. 59 (2008) 332–335.
[36] J. Li, X. Liu, L. Pan, W. Qin, Z. Sun, RSC Adv. 4 (2014) 62387–62392.
[37] F. Chen, Q. Yang, X. Li, G. Zeng, D. Wang, C. Niu, J. Zhao, H. An, T. Xie, Y. Deng, Appl. Catal. B: Environ. 200 (2017) 330–342.
[38] H. Li, D. Zhang, P. Maitarad, L. Shi, R. Gao, J. Zhang, W. Cao, Chem. Commun. 48 (2012) 10645–10647.
[39] L. Huang, X. Zhao, L. Zhang, L. Shi, J. Zhang, D. Zhang, Nanoscale 7 (2015) 2743–2749.
[40] S. Cai, D. Zhang, L. Shi, J. Xu, L. Zhang, L. Huang, H. Li, J. Zhang, Nanoscale 6 (2014) 7346–7353.
[41] S. Luo, T. Nguyen-Phan, A.C. Johnston-Peck, L. Barrio, S. Sallis, D.A. Arena, S. Kundu, W. Xu, L.F.J. Piper, E.A. Stach, D.E. Polyansky, E. Fujita, J.A. Rodriguez, S.D. Senanayake, J. Phys. Chem. C 119 (2015) 2669–2679.
[42] X. Zhang, Z.H. Ai, F.L. Jia, L.Z. Zhang, J. Phys. Chem. C 112 (2008) 747–753.
[43] F. Qin, G. Li, R. Wang, J. Wu, H. Sun, R. Chen, Chem. Eur. J. 18 (2012) 16491–16497.
[44] Y. Xu, M.A.A. Schoonen, Am. Mineral 85 (2000) 543–556.
[45] J. Cao, B. Xu, H. Lin, B. Luo, S. Chen, Dalton Trans. 41 (2012) 11482–11490.
[46] K.S.W. Sing, Pure Appl. Chem. (1985) 603.
[47] J. Xu, W. Meng, Y. Zhang, L. Li, C. Guo, Appl. Catal. B: Environ. 107 (2011) 355–362.
[48] S. Shen, L. Zhao, X. Guan, L. Guo, J. Phys. Chem. Solids 73 (2012) 79–83.
[49] C. Wang, X. Zhang, H. Qiu, G. Huang, H. Yu, Appl. Catal. B: Environ. 205 (2017) 615–623.
[50] H.Z. An, Y. Du, T.M. Wang, C. Wang, W.C. Hao, J.Y. Zhang, Rare Metals 27 (2008) 243–250.
[51] H. Li, J. Shang, Z. Ai, L. Zhang, J. Am. Chem. Soc. 137 (2015) 6393–6399.